



Effects of service environment and pre-deformation on the fatigue behaviour of 2524 aluminium alloy

Y. Q. Chen^{1,2} · H. Zhang^{1,2} · S. P. Pan³ · Y. F. Song^{1,2} · X. Liu² · W. H. Liu^{1,2}

Received: 14 January 2019 / Accepted: 6 October 2019 / Published online: 18 December 2019
© Wrocław University of Science and Technology 2019

Abstract

The effects of service environment and pre-deformation on the fatigue behaviour of 2524 alloy were investigated using scanning electron microscopy (SEM), transmission electron microscopy (TEM), and fatigue tests. The results indicate that the fatigue crack-growth rate (FCGR) of the alloy in an aqueous environment increases with temperature ranging from 0 to 90 °C. At the same stress intensity factor range (ΔK), the FCGR of the alloy in an argon environment is the smallest, followed by that in air, and a 3.5% NaCl fog environment, while that in an exfoliation corrosion (EXCO) solution is the largest. A pre-deformation of 2% can significantly enhance the fatigue crack propagation resistance of this alloy in argon, air, and 3.5% NaCl fog environments, while 5% pre-deformation weakens the fatigue crack propagation resistance of the alloy accordingly. The pre-deformation effect on the FCGR of alloy in the EXCO solution environment is limited.

Keywords 2524 alloy · Service environment · Pre-deformation · Fatigue crack propagation

1 Introduction

Fatigue behaviour has always been a major factor affecting the safety of aviation components, which is changed significantly in different service environments [1, 2], e.g., the crash of flight US ASA 529 in 1995 killed 50 passengers and was caused by the corrosion fatigue of Al alloy components driven by elevated Cl levels in service environments [2]. Besides, the L13 glider fatal accident in Austria in 2010 was also caused by the fatigue damage of aluminium alloy components accelerated by high-temperature exposure [3]. In pursuit of aviation safety, the fatigue damage behaviour of aluminium alloys in different service environments has

always been an important research topic in both material science and engineering.

Previous researches show that the fatigue damage behaviour and mechanisms of aluminium alloys varied significantly in service environments such as salt fog/solution [4], EXCO solution [5, 6], water, etc. Gamboni et al. [7] stated that, in 3.5% NaCl fog environment, the corrosion pit on the surface of Al–Li alloy readily forms a fatigue crack source, which reduces the fatigue resistance of such an alloy. Piascik et al. [8, 9] proposed that the FCGR of the small crack in 2024 alloy in 1.0% NaCl solution is three times higher than that in air. They believed that this is mainly caused by the pitting and microcracking. While Moreto et al. [10] attributed this accelerating effect of 3.5% NaCl fog on FCGR to the corrosion process since it takes place at the vicinity of the crack tip and promotes the evolution of slip bands into microcracks. Besides, an EXCO solution also affects the fatigue properties of aluminium alloys [5, 6]. Ambat et al. [6, 11] found that the corrosion rate of the alloy increases 100-fold when the pH of the environment decreases from 4 to 1. Burns indicated that the degradation in EXCO solution is attributed to the formation of pit clusters on the sample surface [12]; James et al. [13], however, thought that the FCGR of alloy in EXCO solution is mainly influenced by the [H] uptake from corrosion. Li et al. [14] investigated the fatigue behaviours of 2E12 and 7050 alloys in water and

✉ Y. Q. Chen
yqchen1984@163.com

¹ Hunan Provincial Key Laboratory of High Efficiency and Precision Machining of Difficult-to-Cut Material, Hunan University of Science and Technology, Xiangtan 411201, People's Republic of China

² Hunan Provincial Key Defense Laboratory of High Temperature Wear-Resisting Materials and Preparation Technology, Hunan University of Science and Technology, Xiangtan 411201, People's Republic of China

³ School of Materials Science and Engineering, Central South University, Changsha 410083, People's Republic of China

found that hydrogen embrittlement occurs at the crack tip due to local [H] enrichment. Thus, the plasticity of the alloy is decreased, and the fatigue resistance is also reduced; however, another study indicated that oxidation products formed in humid environments lead to the early crack closure and thus decrease the FCGRs, i.e., oxide-induced crack closures (OICC) [15].

Pre-deformation immediately after quenching has long been used to enhance the mechanical properties of aluminium alloy [16]; this increases both the yield strength and tensile strength of aluminium alloy with a slight loss in ductility [17]. The pre-deformation effect on the fatigue properties of aluminium alloy in air was also previously analysed, but no consensus was formed. Yi et al. [18] found that 10% pre-deformation achieved by cold rolling can enhance the fatigue crack propagation resistance in 2E12 aluminium alloy. Jahn et al. [19] indicated that a pre-deformation leads to approximately 20% increase in the fatigue life of 7075 aluminium alloy due to the improvement in strength and the more uniform distribution of fine precipitates. However, Wang et al. [20] thought that the crack-growth rate is only marginally affected by pre-deformation. Chen et al. [21] even found that when the pre-tension strain increases from zero to 4%, the multiaxial fatigue life of 2024 alloy decreases from 17,023 to 7759 cycles.

2524 aluminium alloy is widely used in airframes as a fuselage and wing skin material [22, 23], where the fatigue behaviour is influenced by the external environment, thus, it is essential to understand environmental effects on the fatigue behaviour of 2524 alloy; however, until now, no systematic study of the fatigue crack propagation behaviour of 2524 alloy in different environments has been undertaken. Moreover, it has been found that pre-deformation exerts a significant influence on the fatigue properties of aluminium alloys in air, while the pre-deformation effect on aluminium alloys in different service environments remains unclear. Therefore, an attempt was made to investigate the effects of different service environments and pre-deformation on the fatigue properties of 2524 alloy.

2 Experimental work

The raw material used in this study was a 2.2 mm cold-rolled 2524 alloy plate, with the nominal chemical composition of Al–4.21 Cu–1.41 Mg–0.58 Mn–0.08 Fe–0.06 Si (wt%). The plate was cut into 400 mm × 120 mm pieces which were subjected to solution treatment at 500 °C for 30 min followed by quenching. Immediately, different degrees (0% (T4 temper), 2%, and 5%) of stretching could be applied to these plates using an MTS-Landmark hydraulic servo-controlled test machine. The plate then underwent natural ageing at room temperature for at least 96 h. Then, standard middle-tension M (T) specimens measuring 2.2 mm × 100 mm × 300 mm were produced from the centre of the plate in the L–T orientation (Fig. 1).

The fatigue testing of the specimens under different environments (such as water, argon, 3.5% NaCl fog, and EXCO solution (4.0 M NaCl, 0.5 M KNO₃, 0.1 M HNO₃, pH ~ 0.4), which is usually used to characterise the exfoliation susceptibility of aluminium alloys during fatigue [12]), was carried out on the MTS-Landmark hydraulic servo-controlled test machine equipped with an environmental box, as shown in Fig. 2. A sinusoidal load was applied at a frequency of 10 Hz and a stress ratio ($\sigma_{\min}/\sigma_{\max}$) of 0.1, where σ_{\min} and σ_{\max} represent the minimum and the maximum stresses during

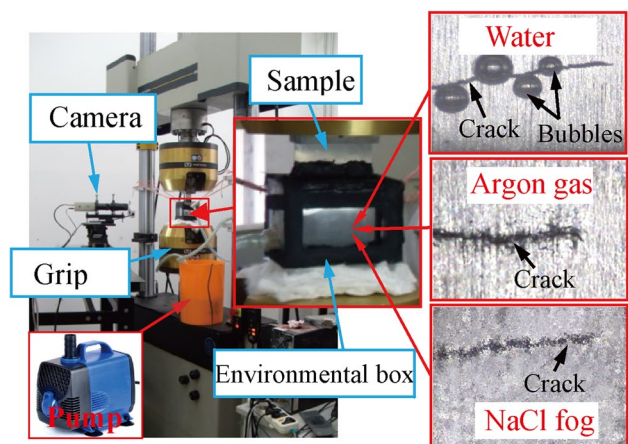
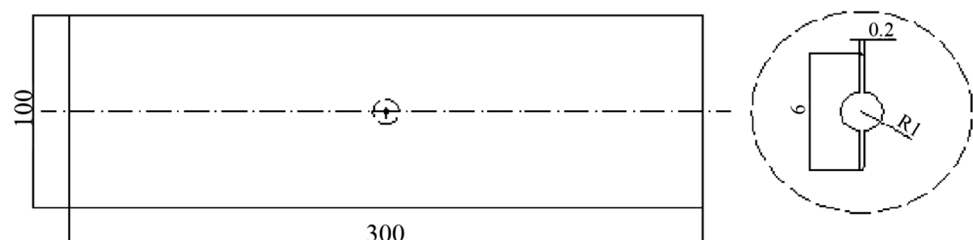


Fig. 2 Experimental equipment for alloy fatigue testing in different environments

Fig. 1 The fatigue crack propagation test specimen (all dimensions, mm)



the loading cycle, respectively. For the fatigue testing of specimens in water and EXCO solution, the distilled water or EXCO solution was poured into a bucket (Fig. 2) where the distilled water or EXCO solution was pumped into an environmental box by a water pump therein and refluxed to the bucket through pipes. To monitor the water temperature, a thermometer was also inserted into the water in the bucket where an electric heater/liquid nitrogen was used to heat/cool the water. For fatigue testing of the specimens in argon and 3.5% NaCl fog environments, the argon or 3.5 wt% NaCl fog was passed through the environmental box, from the argon storage tank or external reservoir and then expelled to the external environment.

The cyclic crack-growth rate, da/dn , was determined from the crack length vs the number of cycles according to ASTM E 647. The length of each fatigue crack was measured using a charge-coupled device (CCD) camera (to $\pm 1 \mu\text{m}$) attached to the fatigue testing apparatus. In situ observation using this camera was also conducted to observe cyclic fatigue crack propagation of the alloy in 3.5% NaCl fog and EXCO solution. The following equation was employed to determine stress intensity factor [24]:

$$\Delta K = \Delta P/B \sqrt{\frac{\pi \alpha}{2w} \sec \frac{\pi \alpha}{2}}, \quad (1)$$

where P is the applied force (in N); B and w represent the thickness (in cm) and width of the specimen, respectively; a denotes the crack length (in cm); and $\alpha = 2a/w$.

Transmission electron microscopy (TEM) and high-resolution transmission electron microscopy (HRTEM) were used to reveal the microstructural changes in the alloy before and after pre-deformation using a Tecnai G²20 TEM, respectively. After fatigue testing, the fatigue fracture morphologies of alloy were also observed using a Quanta-200 environmental SEM equipped with EDAX Genesis (EDS).

3 Results and discussion

3.1 The effect of water environment on fatigue crack-growth behaviour

Figure 3 demonstrates the da/dn curves of 2524-T4 alloy (unpredeformed) in air and water environments at different temperatures. It can be seen that, at the same ΔK , the FCGR of the alloy decreases monotonically with temperature in water. This indicates that a low temperature can delay crack propagation. In the four environments, at the same ΔK , the FCGR of alloy is the largest at 90 °C in water and it is the lowest at 0 °C in water. Besides, at the same temperature of 25 °C, the FCGR of this alloy is higher in water than in air, which suggests that a water environment aids crack

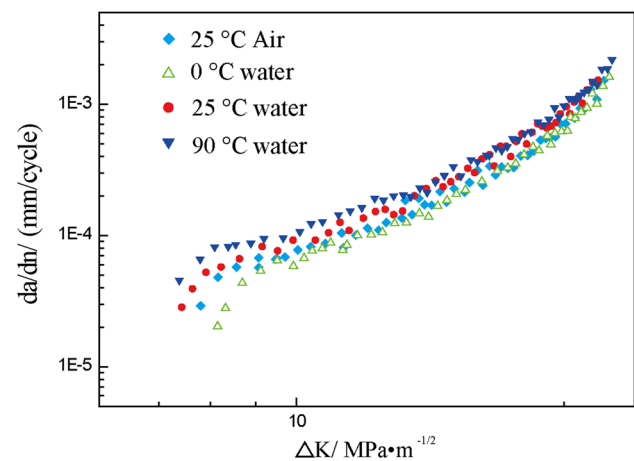


Fig. 3 The da/dn curves of 2524-T4 alloy in air and different water environments

Table 1 Values of ΔK_{th} and ΔK_{cr} of alloy in air and different water environments

Environment	Air	Water at 0 °C	Water at 25 °C	Water at 90 °C
ΔK_{th} (MPa m ^{1/2})	8.2	9.2	7.9	7.4
ΔK_{cr} (MPa m ^{1/2})	20.7	21.3	20.3	20.1

propagation, while, when the temperature is only reduced by 25 °C, the FCGR of alloy in water at 0 °C is lower than that in air. A previous study by Burns et al. [25] found that, when the temperature was changed from 23 to -50 °C, the FCGR of a 7075 aluminium alloy is decreased by nearly an order of magnitude. Our study also supported the fact that the FCGR of alloy is sensitive to temperature and a low-temperature environment can delay crack propagation.

Threshold stress intensity factor range (ΔK_{th}) and critical stress intensity factor range (ΔK_{cr}) are known to be two important design parameters used to evaluate the service security of alloy components. In M (T) specimen, it is very difficult to obtain the conditions for non-propagating cracks due to the presence of the notch. Thus, in the present analysis, ΔK_{th} was defined as the ΔK value at 5×10^{-5} mm/cycle where an optically visible crack has propagated, and ΔK_{cr} was defined as the ΔK value at 10^{-3} mm/cycle where unstable fatigue crack growth usually occurs. To clarify the effects of different environments on the fatigue crack propagation behaviour, the values of ΔK_{th} and ΔK_{cr} obtained from Fig. 3 were evaluated and presented in Table 1; both the values of ΔK_{th} and ΔK_{cr} decrease with the water temperature, while the effect on the ΔK_{th} value is more pronounced. Compared with that in air, the value of ΔK_{th} decreases by about 9.8% at a water temperature of 90 °C and increases by about 12.1% in water at 0 °C, but the change in the ΔK_{cr} value is less

than 3.0% for different water environments compared with those in air. This indicates that the water environments have a greater effect on the early stage of crack propagation than its later stage.

Figure 4 illustrates macroscopic photographs of fatigue cracks in the alloy when loaded in air and different water environments. As is shown in Fig. 4a, the crack in water at

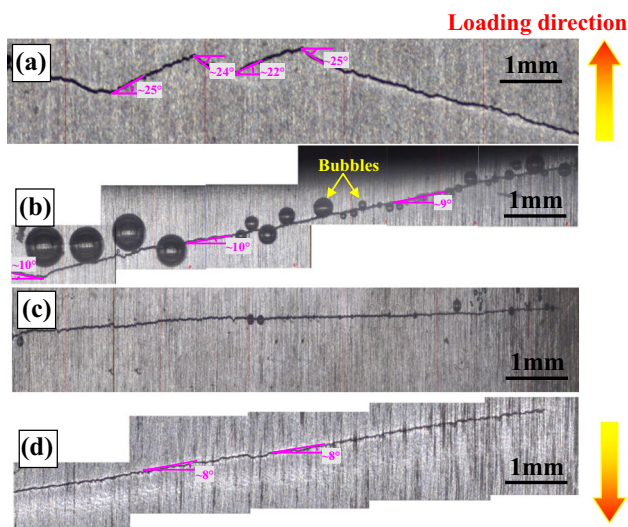
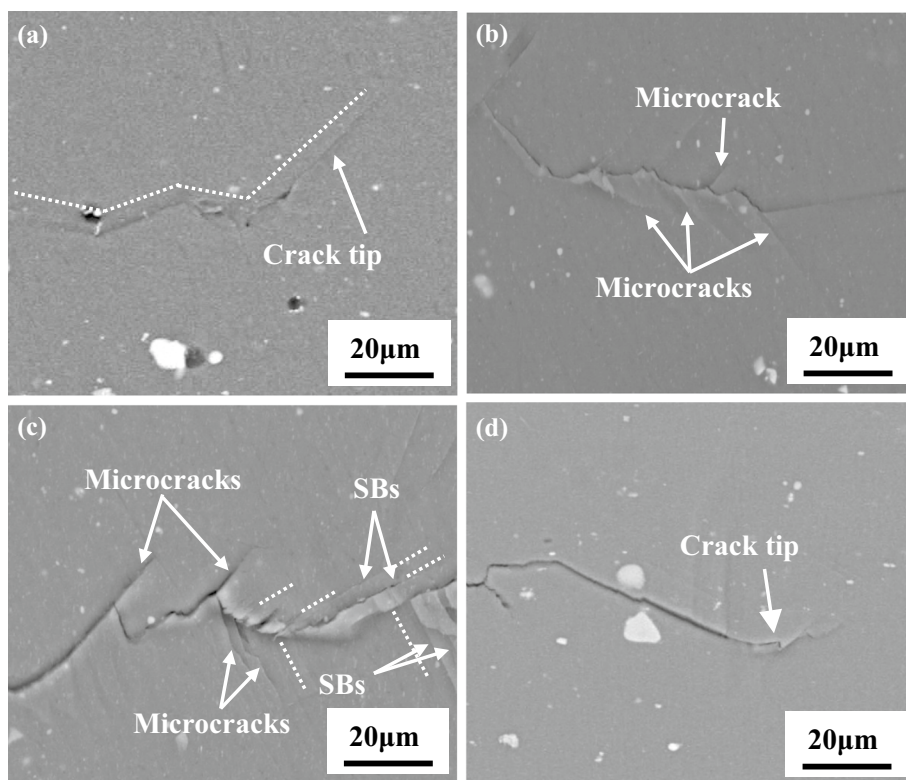


Fig. 4 Macroscopic photographs of fatigue crack growth in air and different water environments **a** 0 °C water, **b** 25 °C water, **c** 90 °C water, **d** 25 °C air

0 °C shows a typical zigzag path, and the angles between each deflected crack path and the horizontal direction are between 22° and 25°. Compared with that in water at 0 °C, the crack in water at 25 °C (Fig. 4b) is relatively straight, but its propagation direction makes a 9°–10° angle in the horizontal direction. The crack in water at 90 °C (Fig. 4c) is straighter and smoother, the path is nearly parallel to the horizontal direction. Figure 4d shows the morphology of the crack in air at 25 °C, which is quite similar to that in water at the same temperature (Fig. 4b). This implies that the water environment has relatively little influence on the macroscopic crack path, but the macroscopic crack path is sensitive to environmental temperature.

Figure 5 shows the SEM images of the crack tip region of the alloy loaded under air and different water temperature conditions at $\Delta K \approx 15 \text{ MPa m}^{1/2}$. As shown in Fig. 5a, the crevice at 0 °C in water is quite narrow and the crack is relatively obscure, which implies that only a small plastic deformation occurs. Different from the crack at 0 °C in water, many microcracks are distributed around the tip region of the crack at 25 °C in water (Fig. 5b) and these microcracks increase in number and extent for alloy specimens loaded at 90 °C in water (Fig. 5c). These results indicate that the embrittlement effect on the crack tip region increases with temperature. As is shown in Fig. 5d, the crack formed at 25 °C in air is also tortuous, but it is neither like that at 0 °C in water which shows apparently zigzag characteristics nor

Fig. 5 SEM images of the crack tip region of 2524 alloy fatigue loaded under air and different water temperature conditions at $\Delta K \approx 15 \text{ MPa m}^{1/2}$ **a** 0 °C water; **b** 25 °C water; **c** 90 °C water; **d** 25 °C air



like those at 25 °C and 90 °C in water which have many microcracks therein.

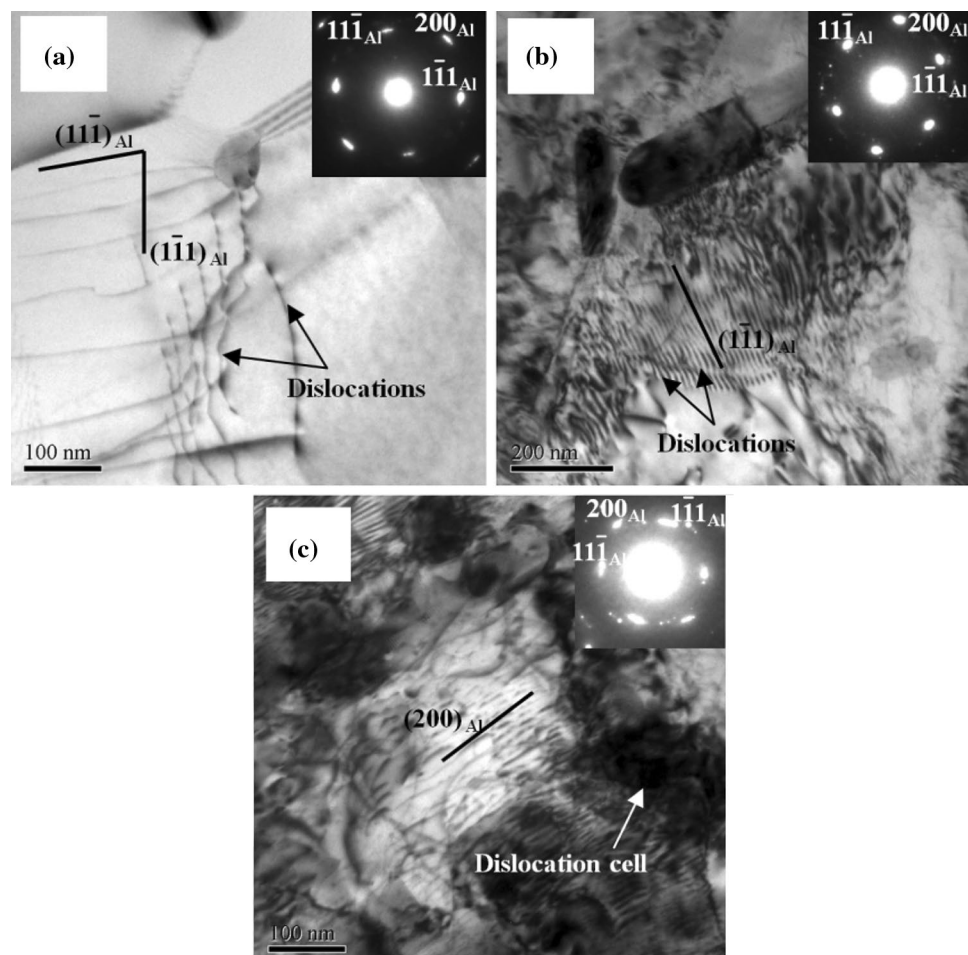
Figure 6 shows the TEM images of the near-fracture-surface-region of alloy loaded in water at different temperatures. As shown in Fig. 6a, when loaded in water at 0 °C, the dislocation density of alloy is quite low. These dislocations are generally parallel to the $\{111\}_{Al}$ planes which sometimes inter-tangled. When loaded in water at 25 °C, the dislocation density of alloy increases significantly. As can be seen in Fig. 6b, a mass of dislocations piled up on the second-phase/matrix interface are still found to be parallel to the $\{111\}_{Al}$ planes, i.e., the main slip planes for aluminium alloys. This phenomenon indicates that, although the dislocation density increases when the temperature increases from 0 to 25 °C, the main slip systems of the alloy do not change. When loaded in water at 90 °C (Fig. 6c), the dislocation density of the alloy further increases and some dislocations are found to lie near the direction of the $\{200\}_{Al}$ planes, which indicates that more slip systems are activated at this elevated temperature.

The effect of water on the fatigue crack propagation behaviour of aluminium alloy is still a matter of debate.

Some studies [26] believed that the water environment effect on the FCGRs of alloy is limited, since hydrogen embrittlement can be counteracted by OICC. OICC is known to be caused by the formation of corrosion debris on the fracture surface, which enhances crack closure during cyclic loading. But other studies [8, 27] show that water environments always significantly accelerate the FCGRs of aluminium alloy due to hydrogen embrittlement. This is confirmed by the results of this study showing that the FCGR of 2524 aluminium alloy is higher in water than in air when loaded at the same temperature. Besides, we found that the water temperature had an even greater impact on the fatigue behaviour of this alloy. This impact not only induced hydrogen embrittlement but also changed the crack path.

During fatigue testing, the crack path depends on both the loading direction and the dislocation slip direction. On the macro-level, the crack always tends to propagate in the direction normal to the loading direction. On the micro-level, a crack is prone to extend along the dislocation slipping direction, i.e. the maximum shear-stress direction (at about 45° to the direction of loading which may be corrected by the Lode angle). These two mechanisms compete with each other.

Fig. 6 TEM images of 2524-T4 alloy at the crack tip regions ($\Delta K \approx 15 \text{ MPa m}^{1/2}$) fatigue loaded at different water temperatures **a** 0 °C; **b** 25 °C; **c** 90 °C



At a low temperature (e.g., 0 °C in water), the crack path is more dependent on the slipping direction since quite limited slip systems exist. Thus, at this temperature, the dislocation slipping effect should play an important role in determining the crack path. As a result of the competition between these two mechanisms, there is a 22°–25° angle between the crack path and horizontal direction in fatigue loading at 0 °C in water (Fig. 4a). Besides which, owing to limited slip systems existing at low temperature, the crack has to extend along a slip plane for a long distance before shifting to another proper slip plane. Each time the crack propagates over a certain long distance, it must turn in the reverse direction which makes it propagate, on the whole, orthogonally to the loading direction. Therefore, the crack follows a macroscopic zigzag path in water at 0 °C. As the temperature increases, the influence of dislocation slipping on the crack path diminishes on account of the increasing number of slip systems, which is also confirmed by Fig. 5c showing more slip bands (SBs) occur in the tip region of crack at 90 °C in water. Therefore, the angle between the crack path and horizontal direction gradually decreases to 9°–10° when loaded in water at 25 °C (Fig. 4b), and further decreases to nearly 0° when loaded in water at 90 °C (Fig. 4c). Since the dislocation motion is easier and the crack path is straighter, the FCGR in water at 90 °C is higher.

A deflected crack can always generate extra length for crack growth which generally decreases the FCGR of alloy to some extent. It is demonstrated in our previous study [18] that, considering the extra length of the crack during deflection, the da/dn value for a deflected crack can be modified thus [24]:

$$\frac{da}{dn} = \left(\frac{D \cos \theta + E}{D + E} \right) \left(\frac{da}{dn} \right)_L \tag{2}$$

where D is the extended distance of tilted crack along the kink (as illustrated in Fig. 7), and E represents the extended

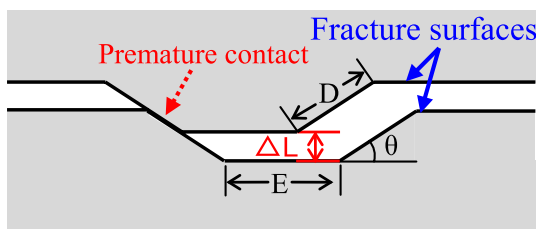


Fig. 7 Schematic representations of crack deflection

distance of the crack on the propagated plane and normal to the loading direction. θ is the kink angle, $(da/dn)_L$ is the FCGR for a straight crack.

Since the E/D value for the crack in Fig. 4 is extremely small, Eq. (2) can be simplified to

$$\frac{da}{dn} = \cos \theta \left(\frac{da}{dn} \right)_L \tag{3}$$

The decreases in da/dn value, caused by the extra length during deflection, were calculated to be only 7.3–9.4% for the crack at 0 °C in water ($\theta=22^\circ\text{--}25^\circ$) and 1.2–1.5% for the crack at 25 °C in water ($\theta=9^\circ\text{--}10^\circ$) according to Eq. (3), but the practical differences between the FCGRs at different water temperatures were measured to be as large as four times those at $\Delta K=8.2 \text{ MPa m}^{1/2}$ and around 70% of those at $\Delta K=15.2 \text{ MPa m}^{1/2}$ (Table 2). This means that the delay for the crack propagated in water at low temperature should not be mainly attributed to the extra length caused by crack deflection but can be mainly attributed to the decrease in hydrogen embrittlement or roughness-induced crack closure (RICC) [28]. As is known, RICC always results in a reduced ΔK value at the crack tip which is caused by the premature contact between mating fracture surfaces in a zigzag-shaped cracks (Fig. 7).

3.2 The effects of argon, NaCl fog, and EXCO solution environments on fatigue crack-growth behaviour

Figure 8 shows the da/dn curves of 2524-T4 alloy in air, argon, 3.5% NaCl fog, and EXCO solution environments, respectively. Compared with the traditional 2024 alloy [29], the 2524-T4 alloy exhibits an approximately 30% smaller FCGR in the early stage of crack propagation when loaded in air. This difference increases with ΔK and finally reaches over two times its original value at $\Delta K > 20 \text{ MPa m}^{1/2}$. As shown in Fig. 8, there are large differences between the FCGRs of 2524-T4 alloy in different environments, especially in the early stage of crack propagation (i.e., low ΔK). When $\Delta K \approx 8 \text{ MPa m}^{1/2}$, the da/dn value of alloy in EXCO solution environment is about $1.1 \times 10^{-4} \text{ mm/cycle}$, which is 46.7% greater than that in 3.5% NaCl fog, two times greater than that in air, and nearly nine times greater than that in argon. With the increase of ΔK , these differences tend

Table 2 The da/dn values of 2524 alloy in air and different water environments at different ΔK

Environment	da/dn values (mm/cycle)		
	$\Delta K=8.2 \text{ MPa m}^{1/2}$	$\Delta K=10.1 \text{ MPa m}^{1/2}$	$\Delta K=15.2 \text{ MPa m}^{1/2}$
0 °C Water	2.01×10^{-4}	4.84×10^{-4}	1.69×10^{-3}
25 °C Water	5.94×10^{-4}	9.16×10^{-4}	2.21×10^{-3}
90 °C Water	8.13×10^{-4}	1.08×10^{-3}	2.87×10^{-3}

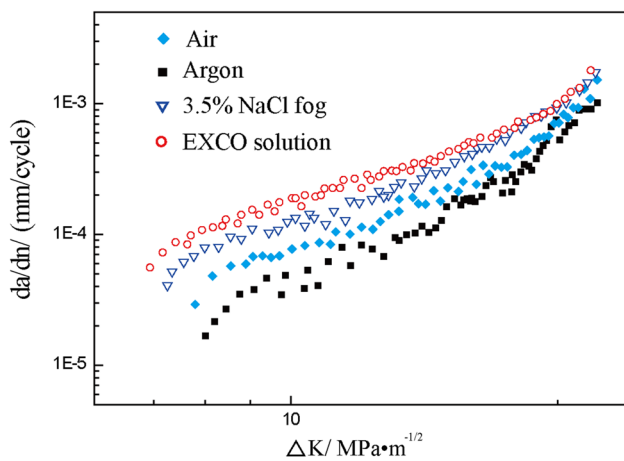


Fig. 8 The da/dn curves of 2524-T4 alloy in different environments

Table 3 Values of ΔK_{th} and ΔK_{cr} of alloy in argon, 3.5% NaCl fog, and EXCO solution environments, respectively

Environment	Argon	3.5% NaCl fog	EXCO solution
ΔK_{th} (MPa m ^{1/2})	9.6	7.3	6.8
ΔK_{cr} (MPa m ^{1/2})	20.9	19.7	19.5

to decrease. At the same ΔK , the FCGR of alloy in an argon environment is the smallest, followed by that in air and 3.5% NaCl fog, while that in an EXCO solution is the largest. It shows that the alloy in argon has the best fatigue properties, while it has the worst fatigue properties in EXCO solution.

Table 3 lists values of ΔK_{th} and ΔK_{cr} of alloy in argon, 3.5% NaCl fog, and EXCO solution environments, respectively. In terms of ΔK_{th} , these environments exert a greater influence on fatigue crack propagation in this alloy than water environments (Table 2). The ΔK_{th} value in argon increases by 17.1% and the ΔK_{th} value in EXCO solution declines by 18.1%, but the influence on the ΔK_{cr} remains limited. This is consistent with previous studies [24, 30] indicating that the fatigue crack-growth behaviour is insensitive to both environment and microstructure.

Figure 9 shows the fatigue fracture morphologies of 2524-T4 alloy in different environments at $\Delta K \approx 15$ MPa m^{1/2}. As shown in Fig. 9a, the fracture morphology of the alloy in air shows apparent crystallographical characteristics in which some small tearing ribs can be observed. In Fig. 9b, the fatigue striations on the alloy are clear, and their width is about 0.17 μ m. The fatigue fracture of alloy in an argon environment shown in Fig. 9c is flatter and smoother compared with that in Fig. 9a which presents a wave-like pattern. The fatigue striations have a width of about 0.11 μ m (Fig. 9d), while not being as evident as those formed in air. This might be due to the more efficient slip reversal in inert environment which impedes the formation of “sharp trenches” at the

fracture surface according to Wanhill [31]. Differing from the fracture morphologies in argon and air environments, a large number of corrosion pits are present on the fatigue fracture surface of the alloy in a 3.5% NaCl fog environment (indicated by white arrows in Fig. 9e). In the inset magnified image, spherical inclusions can be seen just inside the corrosion pits. The width of fatigue striations in Fig. 9f is about 0.29 μ m. Figure 9g shows the fatigue fracture surface of the alloy in EXCO solution. This fracture surface is covered by a thick oxidation film which appears to be obscure. The striations on this surface are indistinguishable; in addition, many quasi-crystalline corrosion products are dispersed over the fracture surface, as indicated by white dashed circles. Table 4 lists the results of EDS analysis on the corrosion product shown in Fig. 9h, which suggests the corrosion products consist of a certain amount of N, Cl, and O.

Figure 10 illustrates macroscopic photographs of fatigue cracks in the alloy when loaded in different environments. In argon (Fig. 10a), the crack path is generally parallel to the horizontal direction, but it is more torturous than that in water at 90 °C (Fig. 4c). Besides, severe plastic deformation regions could be observed at the edge of the crack which indicates that, during crack propagation, the crack tip experiences large deformations. The crack path in 3.5% NaCl fog (Fig. 10b) is similar to that in air (Fig. 4d), but its propagation direction makes an angle of about 7° in the horizontal direction. Besides, there are always some large deflections seen during crack propagation (as indicated by red dotted circles in Fig. 10a). The crack path in EXCO solution (Fig. 10c) is macroscopically straight and almost parallel to the horizontal direction. Many microcracks are found to be formed near the crack tip implying an environmental embrittlement effect.

Figure 11 shows typical SEM images of the crack tip region of 2524 alloy loaded in argon, 3.5% NaCl fog, and EXCO solution. In argon (Fig. 11a), a mass of parallel straight, and uniformly spaced SBs are presented at the crack tip region and some sections of the main crack extend along these SBs (as indicated by dotted box). This indicates that slip plays a dominant role in determining the crack propagation behaviour of this alloy in argon. Besides, due to the strong effect of slip on crack propagation, microscopically, the crack in argon exhibits a zigzag characteristic which makes the crack path more tortuous than that in air (Fig. 5d). In 3.5% NaCl fog (Fig. 11b), the crack shows greater tendency to deflect than in air at 25 °C (Fig. 5d). In addition, many inclusions and corrosion pits can be found distributed on the deflected crack-growth route; this implies that this crack is sensitive to not only the corrosion pit but also the inclusion in front of its path. In EXCO solution (Fig. 11c), the crack displays brittle characteristics namely plentiful microcracks distributed around the crack tip region.

Fig. 9 SEM images of the fatigue fracture surface of 2524-T4 alloy in different environments at $\Delta K \approx 15 \text{ MPa m}^{1/2}$ **a** fracture surface in air shows a rough fractograph, **b** fatigue striation in air, **c** fracture surface in argon indicates a relatively smooth fractograph, **d** fatigue striation in argon, **e** many corrosion pits distributed on the fracture surface in 3.5% NaCl fog, **f** fatigue striation in 3.5% NaCl fog, **g** many corrosion products dispersed over the fracture surface in EXCO solution, **h** fatigue striation in EXCO solution

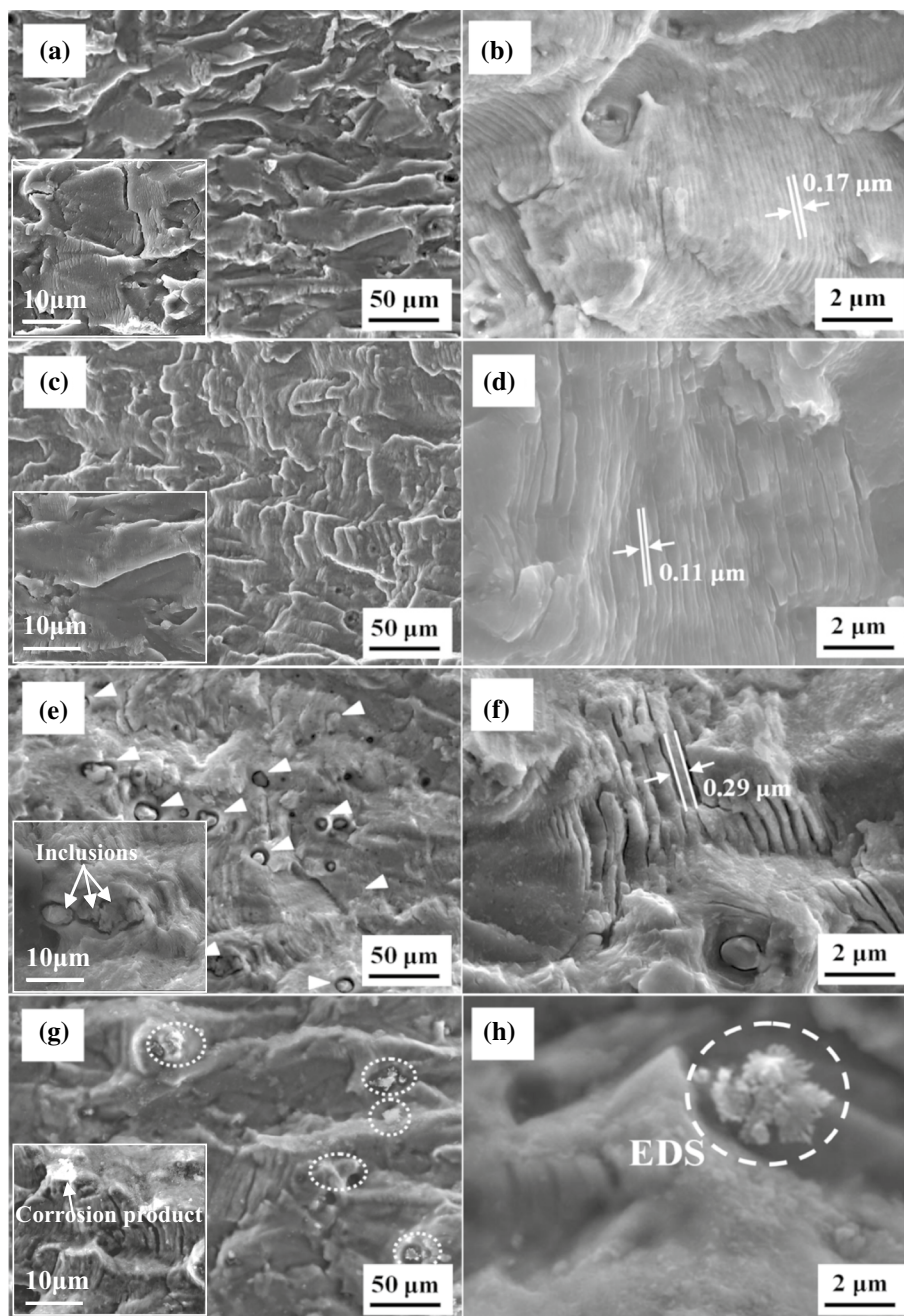


Table 4 Results of EDS analysis on the corrosion product shown in Fig. 9h

Elements	Al	Cu	Mg	Mn	O	Cl	N
Wt%	43.7	27.3	2.4	1.4	15.4	8.5	1.3
At.%	46.9	12.4	2.9	0.7	27.8	6.8	2.5

3.2.1 Argon environment

The effects of inert environments, such as an argon, vacuum, etc., on the fatigue properties of aluminium alloys have been investigated in previous studies [26, 32], most of which indicate that the fatigue crack propagation of aluminium alloys

is significantly delayed in these environments. Investigators recognised that an inert environment can lead to a more uniform, stable SB and more efficient slip-reversal in aluminium alloys compared to those loaded in air due to the absence of oxidation; however, Wanhill et al. [31] found that the difference in the FCGR of 2000 series aluminium alloy in gaseous

Fig. 10 Macroscopic photographs of fatigue crack growth in different environments **a** argon, **b** 3.5% NaCl fog, **c** EXCO solution

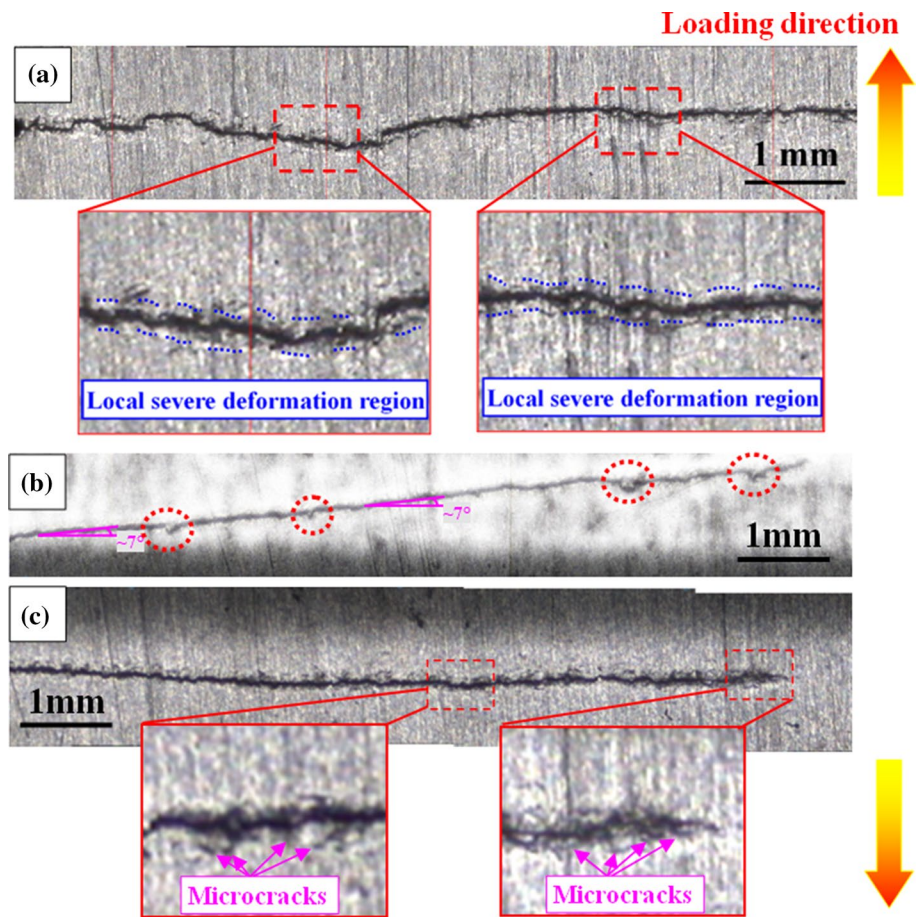
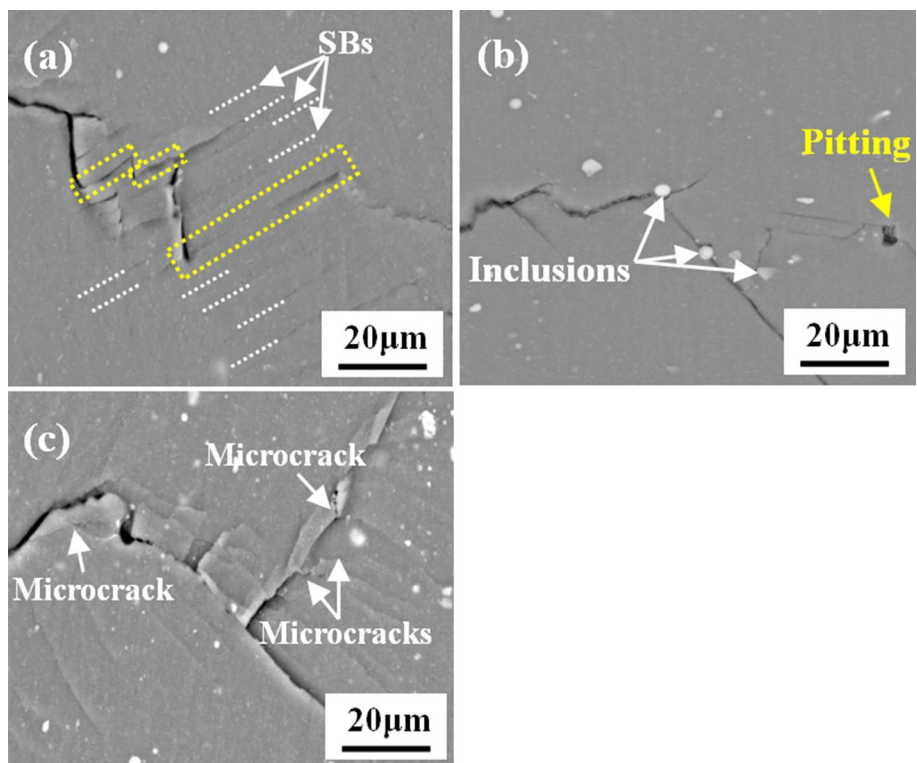


Fig. 11 SEM images of the crack tip region of 2524 alloy fatigue loaded in different environments at $\Delta K \approx 15 \text{ MPa m}^{1/2}$ **a** argon, **b** 3.5% NaCl fog, **c** EXCO solution



oxygen and inert environments (e.g., vacuum and helium) is negligible. They attributed the reason for this to the absence of OICC in inert environments, as OICC is known to reduce the crack driving force and thus slow down the crack growth; however, in our study, we revealed that argon can not only promote the slip during fatigue loading but also increase the microscopic tortuosity of the crack path (or the roughness of the fracture surface). As is known, the oxide film of aluminium alloy fatigue loaded in oxidising environments is less than $0.1 \mu\text{m}$ thick [26] which is extremely small when compared with the scale of the increased crack tortuosity in argon (tens of micron), thus the effect of OICC should be insignificant in comparison with RICC induced by the increased crack tortuosity. Therefore, the FCGR of alloy in argon decreases due to the promotion of uniform slip and RICC.

3.2.2 NaCl fog environment

The 2524 alloy in 3.5% NaCl fog has a higher FCGR than that in air at the same ΔK . This is in agreement with results from other studies [4, 7]. To investigate the accelerating mechanism of NaCl fog on the FCGRs of aluminium alloy, an in situ observation on the propagation behaviour of the crack in 3.5% NaCl fog was carried out (Fig. 12) where both the number of loading cycles and crack length were zeroed. The image in Fig. 12a shows that two large defects (inclusions or corrosion pits) are present, ahead of the crack tip, as indicated by triangles in Fig. 12a. Under cyclic loading, the one in the front induces a microcrack forming at this defect-containing region (Fig. 12c). After 826 cycles, the main crack is propagating slowly towards this microcrack. Again, a new defect forms ahead of the crack tip and it becomes a new microcrack (Fig. 12e). Finally, through coalescence between the main crack and the microcracks, the crack truncates these defect-containing regions after 1263 cycles (Fig. 12g) and 1534 cycles (Fig. 12i), respectively. During these processes, its length suddenly increases to about $99 \mu\text{m}$ and $251 \mu\text{m}$, respectively, which indicates that the local FCGR of aluminium alloy in NaCl fog has a high dependence on the microcrack ahead of the crack tip. Besides, it can also be noticed that the crack propagation in the NaCl fog environment can be considered as an iterative process of microcrack formation and crack coalescence.

To depict the crack propagation mode in NaCl fog, a schematic illustration is provided (Fig. 13). It is generally believed that [4], in a NaCl fog environment, the oxide film forms first which covers the inclusions on the crack surface (Fig. 13a). Since the radii of H^+ and Cl^- are small [7], they can penetrate the oxide film and promote matrix dissolution around the inclusion through galvanic reactions; this leads to interfacial weakening and formation of corrosion pits (Fig. 13b). Previous work [22] shows that, these corrosion

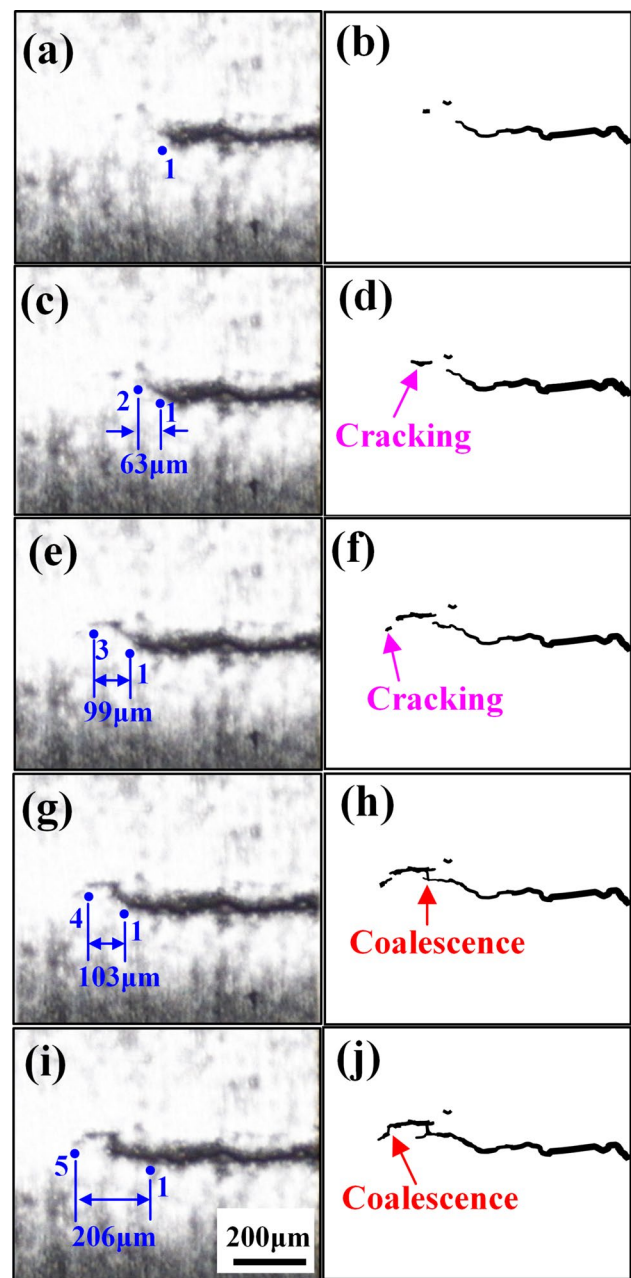
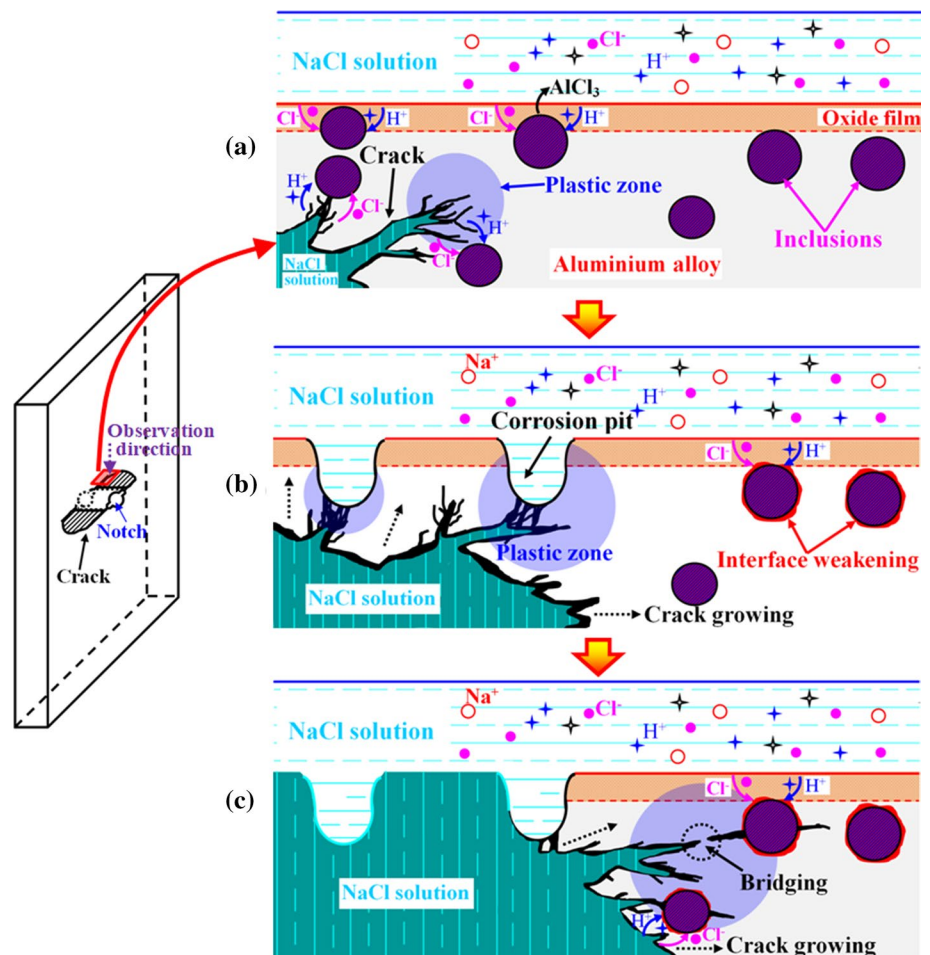


Fig. 12 In situ observation using the CCD camera on the crack ($\Delta K \approx 15 \text{ MPa m}^{1/2}$) in 3.5% NaCl fog environment: **a** no cycles, **b** schematic diagram of **a**, **c** 826 cycles, **d** schematic diagram of **c**, **e** 983 cycles, **f** schematic diagram of **e**, **g** 1263 cycles, **h** schematic diagram of **g**, **i** 1534 cycles, **j** schematic diagram of **i**

pits deflect the crack path and accelerate the FCGRs of aluminium alloys due to local stress concentration, which is confirmed by our observations, but it is further revealed in our study that, besides corrosion pits, the crack propagation is also quite sensitive to the inclusions ahead of the crack tip as the main crack always truncates the inclusion-containing region. In NaCl fog, lots of corrosion pits will form at inclusion sites, but many more inclusions remain

Fig. 13 Schematic diagram of the crack propagation in NaCl fog environment **a** the matrix dissolution surrounding the inclusion by the erosion of H^+ and Cl^- , **b** the interconnection between the crack and corrosion pits, **c** the interconnection between the crack and inclusions with weakly bonded interfaces



in the process of changing into corrosion pits for which the interface with the matrix is weak due to the erosion of H^+ and Cl^- . Both corrosion pits and these inclusions can be regarded as defects which are prone to stress concentration [22]. Thus, during fatigue loading, as the crack tip plastic zone gradually encounters, and finally encompasses, these defects (corrosion pits and inclusions), the formation of microcracks would take place at the defect-containing region ahead of the crack tip. Then, the main crack bridges the microcracks ahead of the crack tip during which the FCGR is accelerated (Fig. 13c).

In Menan et al. work [29] on the fatigue behaviour of 2024 aluminium alloy, the FCGR at $\Delta K \approx 8 \text{ MPa m}^{1/2}$ in 3.5% NaCl fog is increased by nearly three times that in air. Our study revealed that the NaCl fog also accelerates the FCGR of 2524 alloy but the increase in FCGR at $\Delta K \approx 8 \text{ MPa m}^{1/2}$ and $10 \text{ MPa m}^{1/2}$ is less than 60% of the original values (Table 2). This indicates that the 2524 alloy is less sensitive to NaCl fog than 2024 alloy. This might have been due to the relatively lower inclusion density of 2524 alloy, since it contains fewer impurities (such as Fe and Si) than 2024 alloy.

3.2.3 EXCO solution environment

In a previous study [33], it was found that the FCGR of aluminium alloy in the EXCO solution is much greater than that in NaCl solution. Investigators [13] generally attributed the significant deterioration of fatigue properties in EXCO solution to either the embrittlement by hydrogen atoms or formation of corrosion pits. In our observation of the fracture cracking of 2524 alloy in EXCO solution, many crystal-like corrosion products and a thick oxidation film appear on the fracture surface (Fig. 9g), while fewer inclusions or corrosion pits are distributed on the crack-growth route (Fig. 11c) than those in NaCl fog (Fig. 11b). This indicates that the crack propagation behaviour in EXCO solution is not as sensitive to inclusions or corrosion pits as in NaCl fog.

In situ observation of the propagation behaviour of the crack in EXCO solution was undertaken (Fig. 14); both the number of loading cycles and crack length were zeroed. As shown in Fig. 14a, each fatigue crack in EXCO solution has many branches and several microcracks are formed ahead of the crack tip. After 543 cycles, the main crack quickly bridges two of these microcracks during which its length

increases by 285 μm . Besides, at the region beneath the crack, some microcracks also nucleate (Fig. 14b). Then, after 813 cycles, several microcracks nucleate again ahead of the crack tip (Fig. 14c). It is clear that the propagation of the crack in EXCO solution is discontinuous because of the nucleation of microcracks in front of it and bridging connections therewith, but it should be pointed out that, except for those microcracks immediately ahead of the tip of the main crack, the crack is also inclined to connect with those above and below the tip of the main crack (e.g., the microcracks below the crack tip are also coalesced by the main crack, as indicated by the dotted circle in Fig. 14c). This accounts for the many branches of the crack in EXCO solution and it also implies the severe fragility of the crack tip region in EXCO solution which is probably induced by hydrogen embrittlement. In short, our study shows that crack propagation in 2524 aluminium alloy is more susceptible to hydrogen embrittlement than corrosion pitting.

3.3 The effect of pre-deformation on the fatigue behaviour of 2425 alloy

Table 5 summarises the mechanical properties of alloy after different pre-deformation levels: as can be seen, with the increase of pre-deformation from 0 to 2%, both the yield strength ($\sigma_{0.2}$) and ultimate tensile strength (σ_u) of the alloy increase, although moderately compensated by a loss of 1.3% in the elongation (δ). Compared with specimens subjected to 2% pre-deformation, the strengths of alloy specimens with 5% pre-deformation increase notably, but their values of δ decrease significantly.

Figure 15 shows the da/dn curves of 2524-T4 alloy with different pre-deformations in air, argon, 3.5% NaCl fog, and EXCO solution environments, respectively. As shown in Fig. 15a, in air, the da/dn values of the alloy with 2% pre-deformation are the lowest. This indicates that 2% pre-deformation can impede crack propagation, while, when the pre-deformation increases to 5%, the da/dn values increase significantly and are higher than those with no pre-deformation. Similar results were also observed in alloy specimens loaded in argon (Fig. 15b) and 3.5% NaCl fog (Fig. 15c) environments, but the differences in da/dn values caused by

Table 5 The mechanical properties of alloy after different degrees of pre-deformation

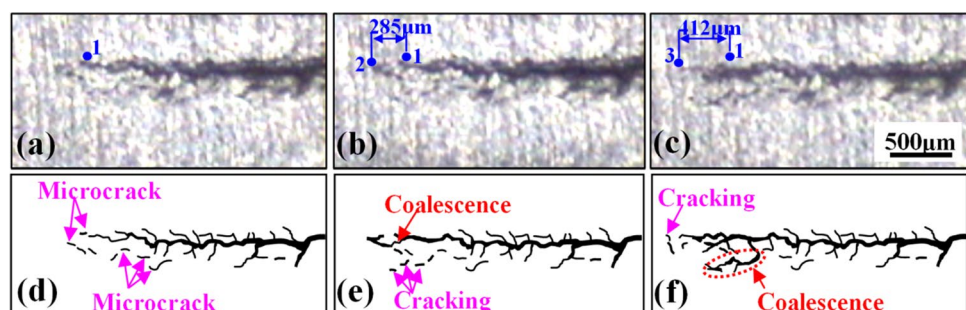
Specimen	$\sigma_{0.2}$ (MPa)	σ_u (MPa)	δ (%)
0% Stretch	289.4	357.7	25.8
2% Stretch	305.8	365.2	24.5
5% Stretch	327.3	385.2	20.1

pre-deformation are more pronounced in an argon environment; however, this difference almost vanishes in the EXCO solution (Fig. 15d), which means that pre-deformation has little effect on the fatigue crack propagation behaviour of alloy in an EXCO solution environment. Besides, it is shown that, the da/dn values in argon are more scattered than those in the other three environments tested. This might be due to the more tortuous crack path formed in argon which increases the dispersion of FCGR.

Figure 16 shows the microstructure of 2524 alloy after different pre-deformations. It is found that there is no apparent precipitate in these alloys but a large number of short rod-shaped T-phase particles [34] exist within the matrix (Fig. 16a). These T-rods are known to be the main dispersoids in this type of alloy which are believed to be formed during the homogenisation process after casting [35]. For the unstretched specimen, the dislocation density is quite low (Fig. 16a) shows a large number of ellipsoidal GP zones [36, 37] with a mean average size of 3.52 ± 0.23 nm distributed homogeneously in the matrix (Fig. 16b). With the increase of pre-deformation to 2%, the dislocation density increases (Fig. 16c), and these dislocations are generally uniformly distributed in the matrix. Besides, the GP zone density of the specimen after 2% pre-deformation increases but their average size decreases to 3.08 ± 0.18 nm (Fig. 16d). When the pre-deformation increases to 5%, the distribution of dislocations becomes non-uniform, and some parallel dislocation walls (Fig. 16e) and abnormally grown GP zones (as shown by the white triangles in Fig. 16f) can be seen in the matrix.

Previous studies [38, 39] found that pre-deformation enhances the fatigue properties of alloys in air. The main reason for this is that, the dislocations increase with the pre-deformation, which function as barriers to subsequent

Fig. 14 In situ observation by CCD camera ($\Delta K \approx 15 \text{ MPa m}^{1/2}$) in EXCO solution for different numbers of loading cycles **a** 0 cycle, **b** 543 cycles, **c** 813 cycles, **d** schematic diagram of **a**, **e** schematic diagram of **b**, **f** schematic diagram of **c**



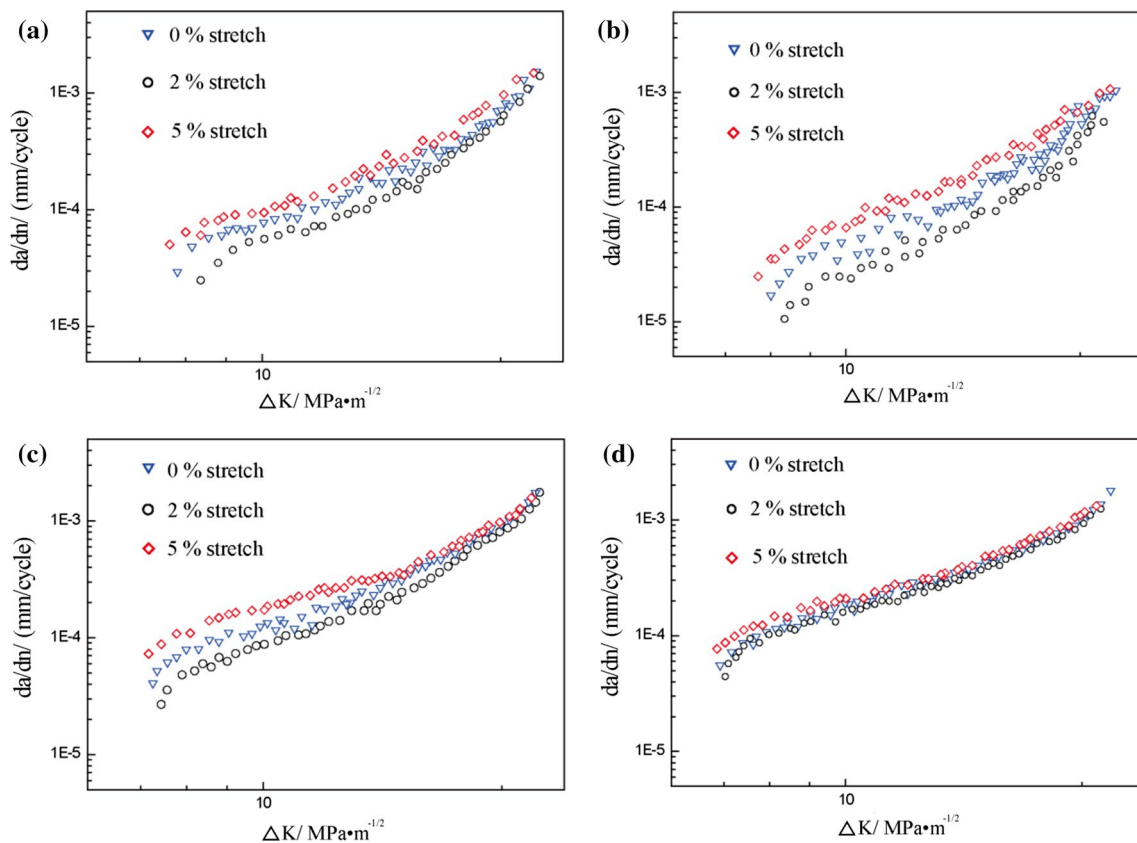


Fig. 15 The da/dn curves of pre-deformed 2524-T4 alloy in different environments **a** air, **b** argon, **c** 3.5% NaCl fog, **d** EXCO solution

dislocation motion during fatigue loading [40], and thus delaying crack initiation and impeding crack propagation. This is in agreement with the findings of our study in the specimen with 2% pre-deformation which has a higher dislocation density, and a higher crack-growth resistance than that with no pre-deformation when fatigue loaded in air. Besides, it is also found that, the uniformly distributed dislocations introduced by 2% pre-deformation produce finer GP zones in the matrix than those in non-predeformed specimens. This can intensify the interaction between GP zones and dislocations, and therefore decrease the average slip distance during each loading cycle.

As shown in our study, the crack propagation in an argon environment is more dependent on dislocation slip than that in air; due to the reduction in slip distance during each loading cycle, the decrease in the FCGRs of alloy in argon caused by 2% pre-deformation is also more evident than that in air.

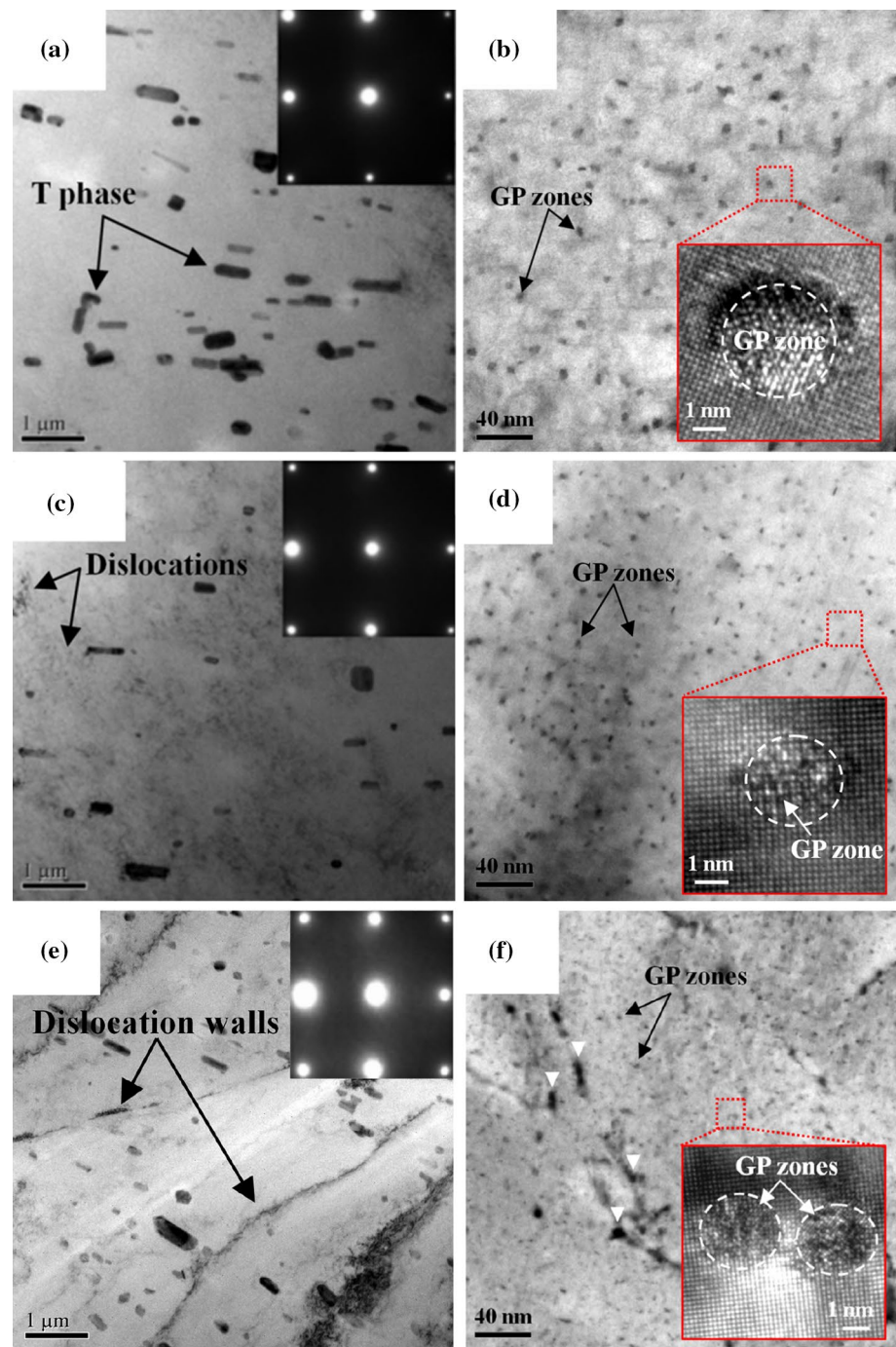
In a 3.5% NaCl fog environment, crack propagation is susceptible to corrosion pitting and the weakly bonded inclusions formed by corrosion since they cause stress concentrations ahead of the crack tip. Thus, the fatigue properties of this alloy in NaCl fog can be improved by the enhancement of corrosion resistance as well as stress concentration

resistance. For the 2% pre-deformed specimen, the refinement of GP zones enhances the corrosion resistance to a certain extent. Besides, the increase in $\sigma_{0.2}$ enhances the resistance to stress concentration. Both these effects result in the decrease of the FCGRs of 2% pre-deformed specimens in NaCl fog environment.

As mentioned, the crack propagation of this alloy in EXCO solution is mainly susceptible to hydrogen embrittlement induced by the presence of sufficiently concentrated hydrogen atoms in the Al lattice. It is known that, since the atomic radius of hydrogen is much smaller than those of Al, hydrogen atoms can either diffuse into the bulk material or be transported by dislocation cores [41]. The large number of dislocations produced by pre-deformation can provide a mass of channels for H-transportation, which aggravates the hydrogen embrittlement in the alloy and counteracts the beneficial effects of pre-deformation on the fatigue crack resistance. Therefore, differing from those in air, argon, and a 3.5% NaCl fog environments, the pre-deformation effect on the FCGRs of alloy in EXCO solution environment is quite limited.

When the amount of pre-deformation is increased to 5%, the dislocation distribution in the alloy becomes non-uniform and many dislocation walls with high densities of

Fig. 16 TEM images, corresponding selected-area electron diffraction patterns (SAEDP) and HRTEM images of 2524 alloy after different pre-deformations viewed along the $\langle 010 \rangle_{Al}$ axis **a** the dislocation distribution and **b** GP zones of alloy specimens with 0% pre-deformation; **c** the dislocation distribution and **d** GP zones of alloy specimens with 2% pre-deformation; **e** the dislocation distribution and **f** GP zones of alloy specimens with 5% pre-deformation



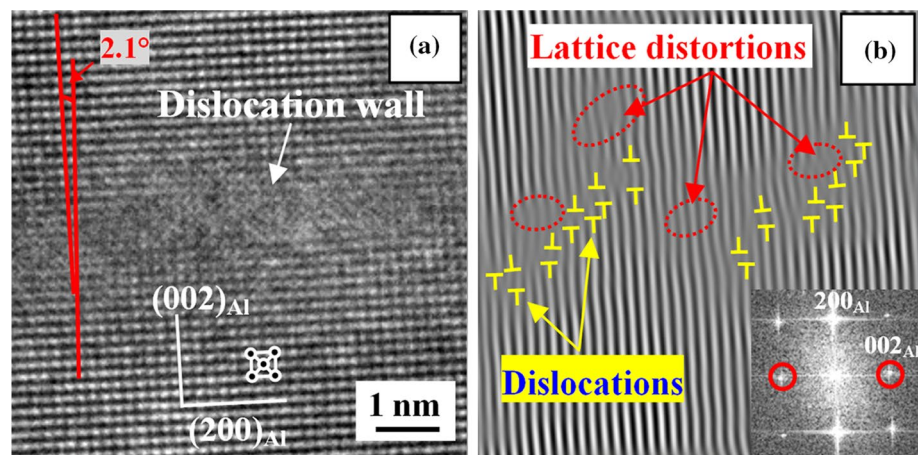
dislocation and lattice distortions can be seen in the matrix (Fig. 17). Wu et al. [42] investigated the pre-stretching effect on the microstructure of an artificial aged 2024 aluminium alloy, finding that, when the pre-stretch exceeds 2.0%, it can induce an uneven distribution of both dislocations and second-phase particles. Inhomogeneous deformation produced by 5% pre-deformation can be thought of as microscopic damage. It inevitably leads to a loss of ductility reflected in the significant decrease in δ (Table 5). As predicted, such microscopic damage can provide source loci for both crack

initiation and corrosion pitting, therefore, the specimen with 5% pre-deformation has the worst fatigue properties among those specimens studied here.

4 Conclusion

1. When loaded at the same temperature of 25 °C, the FCGR is larger in water than that in air at the same ΔK . In water, between 0 and 90 °C, the FCGR of 2524 alloy

Fig. 17 **a** The typical HRTEM images of a dislocation wall in the specimen with 5% pre-deformation viewed along the $\langle 010 \rangle_{\text{Al}}$ axis, **b** inverse fast-Fourier-filtered (IFFT) image indicating that a large number of dislocations and significant lattice distortions are present in the dislocation wall region (the inset shows the corresponding fast-Fourier-filtered (FFT) image)



- increases with increasing water temperature due to the increase in hydrogen embrittlement and the decreases in fracture surface roughness.
2. An argon environment hinders the FCGRs of 2524 alloy due to the promotion of uniform slip and RICC induced by increased crack tortuosity.
 3. The fatigue crack propagation of 2524 alloy is accelerated in NaCl fog: this can be regarded as two repeated processes, i.e., microcrack formation at the defect (inclusion or corrosion pit)-containing region ahead of the crack tip and the coalescence between the main crack and the microcracks. The local FCGR is accelerated during crack coalescence.
 4. The FCGR of 2524 alloy in EXCO solution is the fastest among argon, air, NaCl fog, and EXCO solution environments at the same ΔK , which is mainly attributed to the severe fragility of the crack tip region as induced by hydrogen embrittlement.
 5. A pre-deformation of 2% can improve the fatigue crack propagation resistance in air, argon, and 3.5% NaCl fog environments, due to the moderately enhanced strength, limited loss of δ , and refinement of GP zones; however, 5% pre-deformation accelerates the FCGRs of alloy in air, argon, and 3.5% NaCl fog environments, due to the associated microscopic damages and decrease in δ .
 6. The pre-deformation effect on the FCGRs of alloy in an EXCO solution environment is limited due to the counteractive strength enhancing, and hydrogen embrittlement effects.

Acknowledgements This work was supported by the National Natural Science Foundation of China (Grant nos. 51405153 and 51875197).

Compliance with ethical standards

Conflict of interest No conflict of interest exists in the submission of this manuscript, and the manuscript is approved for publication by all the authors' concern.

Ethical statement I would like to declare on behalf of my co-authors that the work described is original research that has not been published previously, and is not currently under consideration for publication elsewhere, in whole or in part. All the authors listed have approved the manuscript that is enclosed.

References

1. Shou WB, Yi DQ, Liu HQ, Tang C, Shen FH, Wang B. Effect of grain size on the fatigue crack growth behavior of 2524-T3 aluminum alloy. *Arch Civ Mech Eng*. 2019;19:287–96.
2. Patankar MS, Taylor JC. MRM training, evaluation, and safety management. *Int J Aviat Psychol*. 2008;18(1):61–71.
3. Nováková L, Boháčová M, Homola P. Application of material analysis and eddy current conductivity tests to aircraft accident investigation. *Eng Fail Anal*. 2015;56:422–8.
4. Kermanidis AT, Zervaki AD, Haidemenopoulos GN, Pantelakis SG. The influence of salt fog exposure on the fatigue performance of Alclad 6xxx aluminum alloys laser beam welded joints. *J Mater Sci*. 2010;45(16):4390–400.
5. Vasco MC, Chamos AN, Pantelakis SG. Effect of environment's aggressiveness on the corrosion damage evolution and mechanical behavior of AA 2024-T3. *Fatigue Fract Eng Mater Struct*. 2017;40(7):1551–61.
6. Song H, Bai Z, Zhang H, Niu Y, Leen SB. Effect of pre-corrosion on damage evolution and crack propagation in aluminum alloy 7050-T7651. *Fatigue Fract Eng Mater Struct*. 2018;41:2376–90.
7. Gamboni OC, Moreto JA, Bonazzi LHC, Ruchert COFT, Filho BWW. Effect of salt-water fog on fatigue crack nucleation of Al and Al–Li alloys. *Mater Res*. 2014;17(1):250–4.

8. Zhu X, Jones JW, Allison JE. Effect of frequency, environment, and temperature on fatigue behavior of E319 cast-aluminum alloy: small-crack propagation. *Metall Mater Trans A*. 2008;39(11):2666–80.
9. Piascik RS, Willard SA. The growth of small corrosion fatigue cracks in alloy 2024. *Fatigue Fract Eng Mater Struct*. 2010;17(11):1247–59.
10. Moreto JA, Broday EE, Rossino LS, Fernandes JCS, Bose Filho WW. Effect of localized corrosion on fatigue–crack growth in 2524-T3 and 2198-T851 aluminum alloys used as aircraft materials. *J Mater Eng Perform*. 2018;27(4):1917–26.
11. Ambat R, Dwarakadasa ES. The influence of pH on the corrosion of medium strength aerospace alloys 8090, 2091 and 2014. *ChemInform*. 1992;23(26):681–90.
12. Burns JT, Kim S, Gangloff RP. Effect of corrosion severity on fatigue evolution in Al–Zn–Mg–Cu. *Corros Sci*. 2010;52(2):498–508.
13. Burns JT, Gangloff RP. Effect of low temperature on fatigue crack formation and microstructure-scale growth from corrosion damage in Al–Zn–Mg–Cu. *Metall Mater Trans A*. 2013;44:2083–105.
14. Li K, Xiong J, Ma S, Chen B. Contrast tests on fatigue properties of aluminum alloys 2E12-T3 and 7050-T7451 in pudding environment of fuel tank. *J Aeronaut Mater*. 2017;37(01):65–72.
15. Suresh S, Zamiski F, Ritchie RO. Oxide-induced crack closure: an explanation for near-threshold corrosion fatigue crack growth behaviour. *Metall Trans A*. 1981;12:1435–43.
16. An L, Cai Y, Liu W, Liu S, Zhu SQ, Meng FC. Effect of pre-deformation on microstructure and mechanical properties of 2219 aluminum alloy sheet by thermomechanical treatment. *Trans Nonferr Met Soc China*. 2012;22(2):370–5.
17. Wang H, Yi Y, Huang S. Influence of pre-deformation and subsequent ageing on the hardening behavior and microstructure of 2219 aluminum alloy forgings. *J Alloys Compd*. 2016;685:941–8.
18. Yi DQ, Yang S, Deng B, Zhou MZ. Effect of pre-strain on fatigue crack growth of 2E12 aluminum alloy. *Trans Nonferr Met Soc China*. 2007;17(1):141–4.
19. Jahn MT, Jen MBG. Effects of TAHA treatments on the fatigue life of a 7075 aluminum alloy. *J Mater Sci*. 1986;21:799–802.
20. Wang GS, Blom AF. Effect of large local plastic flow on the fatigue life of metallic materials. *Radiology*. 2005;107(3):711–2.
21. Chen Y, Zhou J, Liu C, Wang F. Effect of pre-deformation on the pre-corrosion multiaxial fatigue behaviors of 2024-T4 aluminum alloy. *Int J Fatigue*. 2018;108:35–46.
22. Shen F, Yi D, Jiang Y, Wang B, Liu H, Tang C, Jiang B. Semi-quantitative evaluation of texture components and anisotropy of the yield strength in 2524 T3 alloy sheets. *Mater Sci Eng A*. 2016;675:386–95.
23. Majzoobi GH, Kashfi M, Bonora N, Iannitti G, Ruggiero A, Khademi E. Damage characterization of aluminum 2024 thin sheet for different stress triaxialities. *Arch Civ Mech Eng*. 2018;18:702–12.
24. Yin D, Liu H, Chen Y, Yi D, Wang B, Wang B, Shen F, Fu S, Tang C, Pan S. Effect of grain size on fatigue-crack growth in 2524 aluminium alloy. *Int J Fatigue*. 2016;84:9–16.
25. Burns JT, Gupta VK, Agnew SR, Gangloff RP. Effect of low temperature on fatigue crack formation and microstructure-scale propagation in legacy and modern Al–Zn–Mg–Cu alloys. *Int J Fatigue*. 2013;55(7):268–75.
26. Vasudévan AK, Suresh S. Influence of corrosion deposits on near-threshold fatigue crack growth behavior in 2xxx and 7xxx series aluminum alloys. *Metall Trans A*. 1982;13(12):2271–80.
27. Tong ZX, Lin S, Hsiao CM. The influence of water vapor on the fatigue crack propagation kinetics in pure aluminum single crystals. *Metall Trans A*. 1989;20(5):925–33.
28. Pokluda J. Dislocation-based model of plasticity and roughness-induced crack closure. *Int J Fatigue*. 2013;46(1):35–40.
29. Menan F, Henaff G. Influence of frequency and exposure to a saline solution on the corrosion fatigue crack growth behavior of the aluminum alloy 2024. *Int J Fatigue*. 2009;31:1684–95.
30. Chen YQ, Zhang H, Song WW, Pan SP, Liu WH, Liu X, Zhu BW, Song YF, Zhou W. Acceleration effect of a graphite dust environment on the fatigue crack propagation rates of Al alloy. *Int J Fatigue*. 2019;126:20–9.
31. Wanhill RJH. Fractography of fatigue crack propagation in 2024-T3 and 7075-16 aluminum alloys in air and vacuum. *Metall Trans A*. 1975;6(8):1587–96.
32. Piascik RS, Gangloff RP. Environmental fatigue of an Al–Li–Cu alloy: part I. Intrinsic crack propagation kinetics in hydrogenous environments. *Metall Trans A*. 1991;22:2415–28.
33. Zhang X, Wang HW, Xu S, He W. Investigation on corrosion behaviors of aluminum alloy in NaCl and EXCO solution, multi-discipline model. *Mater Struct*. 2013;9(3):359–66.
34. Chen YQ, Pan SP, Liu WH, Liu X, Tang CP. Morphologies, orientation relationships, and evolution of the T-phase in an Al–Cu–Mg–Mn alloy during homogenisation. *J Alloys Compd*. 2017;709:213–26.
35. Chen YQ, Pan SP, Zhu BX, Liu X, Liu WH, Tang CP. The evolution of orientation relationships during the transformation of a twin-free T-particle to tenfold T-twins in an Al alloy during homogenisation. *Mater Charact*. 2018;141:59–73.
36. Chen JQ, Liu C, Lia QL, Zhao HJ. A three-dimensional characterization method for the preferentially oriented precipitation of Ω -phase in stress-aged Al–Cu–Mg–Ag single crystal. *Mater Charact*. 2019;153:184–9.
37. Chen JQ, Deng YL, Guo XB. Revisit the stress-orienting effect of θ' in Al–Cu single crystal during stress aging. *Mater Charact*. 2018;135:270–7.
38. Zhang XL, Xu X, Ling ZY, Wei J, Cheng T, Zhao JJ. Effect of pre-deformation on microstructure and properties of ultra-high strength aluminum alloy extrusion materials. *Chin J Nonferr Met*. 2016;26(3):507–15.
39. Li C, Zheng X, Dan Z, Tian Y, Song J, Chen L. Effects of pre-deformation on microstructure and mechanical properties of semi-solid 7075 alloy. *Heat Treat Met*. 2016;41(2):127–31.
40. Chen JQ, Li SC, Cong HL, Yin ZM. Microstructure and mechanical behavior of friction stir-welded Sc-modified Al–Zn–Mg alloys made using different base metal tempers. *J Mater Eng Perform*. 2019;28:916–25.
41. Song RG, Dietzel W, Zhang BJ, Liu WJ, Tseng MK, Atrens A. Stress corrosion cracking and hydrogen embrittlement of an Al–Zn–Mg–Cu alloy. *Acta Mater*. 2004;52:4727–43.
42. Wu J, Guo R, Li H, Zhang S. Effects of biaxial pre-stretching on microstructures and mechanical properties of 2024 aluminum alloy thin plates. *Appl Mech Mater*. 2014;472:607–11.

Publisher's Note Springer Nature remains neutral with regard to jurisdictional claims in published maps and institutional affiliations.